Ceramics International 49 (2023) 6713–6719

Contents lists available at ScienceDirect

Ceramics International

journal homepage: www.elsevier.com/locate/ceramint

Enhanced mechanical properties of CrN coatings by plasma immersion ion implantation and deposition

Liangliang Liu [a,1], Tijun Li [b,1], Qingdong Ruan [a], Dan Li [a], Chao Huang [a], Xiaolin Zhang [a], Yinghe Ma [a], Yuzheng Wu [a], Zhongcan Wu [b], RickyK.Y. Fu [a], Zhongzhen Wu [b,*], Paul K. Chu [a,**]

[a] Department of Physics, Department of Materials Science and Engineering, and Department of Biomedical Engineering, City University of Hong Kong, Tat Chee Avenue, Kowloon, Hong Kong, China

[b] School of Advanced Materials, Peking University Shenzhen Graduate School, Shenzhen, 518055, China

ARTICLE INFO

Keywords:
Crystal defects
Ion energy
CrN coatings
Mechanical properties
PIII&D
Plasma immersion ion implantation and deposition

ABSTRACT

Crystal defects can enhance the properties of materials without changing the composition but introduction of high-density defects in coatings is challenging. Herein, plasma immersion ion implantation and deposition (PIII&D) is employed to produce high-density crystal defects in CrN coatings to improve the mechanical properties. PIII&D is demonstrated to introduce high-density point defects and stacking faults into the CrN coatings, especially at a bias exceeding 10 kV. The dislocation density significantly increased from $5.2 \times 10^{14}/m^2$ to $1.3 \times 10^{17}/m^2$. In addition, the covered area of defects increased from 30% to 75% with the ion implantation. As a result, the hardness increases significantly from 24.2 GPa to 35.6 GPa, while the fracture toughness is not compromised.

1. Introduction

Higher hardness is preferred in many tribological applications and one of the desirable features of coatings technology [1,2]. Crystal defects have been observed to strengthen metallic materials without changing the composition [3–5]. Generally, crystal defects such as dislocations, stacking faults, and special grain boundaries can be produced by applying shear stress during repeated rolling and forging [6,7]. However, those methods are difficult for ceramic coatings due to the inherent brittleness and small coating thickness.

Defects in hard coatings can be created and controlled by the deposition process. According to *H. Windischmann,* generation and annihilation of defects are accompanied by intrinsic stress [8] which can be tailored by ion bombardment [9]. When optimizing the ion bombardment by adjusting the bias, *Xu* et al. have found that high-density crystal defects can be created around coherent/semi-coherent grain boundaries between grains with different orientation [10]. *Liu* et al. have increased the defect zone by 10 times by repeatable engineering of coherent/semi-coherent grain boundaries [11] but only about 3% of the thickness is affected. Ion implantation can introduce energetic ions into materials to create lattice defects [12] and the coating hardness can indeed be improved by ion implantation [13,14]. However, the relationship between hardening and crystal defects is still not well understood. Ion implantation is commonly performed after coating deposition using metal vapor vacuum arc (MEVVA) ion sources and so the implantation depth is generally quite small (several tens to hundreds of nanometers) [15,16] in comparison with the total coating thickness which is typically on the order of micrometers. In addition, the MEVVA equipment is complex and expensive. In this respect, plasma immersion ion implantation and deposition (PIII&D) employing the filtered cathode vacuum arc (FCVA) as the ion source can provide ion implantation during coating deposition by simply applying a negative pulsed bias to the sample [17]. The FCVA could produce higher density ions which is more efficient compared with MEVVA. Besides, the ions could be implanted into materials at the function of bias, which would significantly simplify the equipment. Therefore, this technique has high adaptability and efficiency from the perspective of defect engineering of coatings.

In this work, different pulsed biases are used in PIII&D to deposit CrN coatings and create defects. The effects of the ion energy on the

* Corresponding author.
** Corresponding author.
E-mail addresses: liull620@163.com (L. Liu), wuzz@pkusz.edu.cn (Z. Wu), paul.chu@cityu.edu.hk (P.K. Chu).
[1] The authors make equal contributions.

https://doi.org/10.1016/j.ceramint.2022.10.215
Received 4 August 2022; Received in revised form 2 October 2022; Accepted 17 October 2022
Available online 19 October 2022

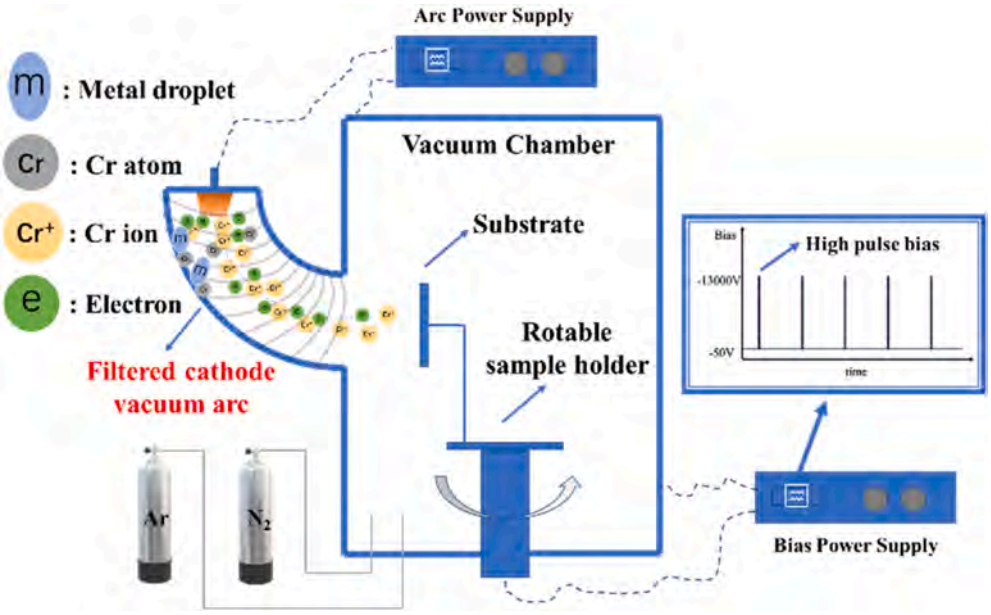

Fig. 1. Schematic showing the ion implantation and deposition equipment.

Table 1
Important processing parameters.

Sample	DC bias(V)	Pulse Bias		
		Pulse length (μs)	Frequency (Hz)	Voltage (V)
D-50	−50	–	–	–
P-3000	−50	20	25	−3000
P-8000	−50	20	25	−8000
P-13000	−50	20	25	−13000

production of crystal defects and relationship between defects and mechanical properties of the coatings are investigated. The results show that high-density dislocations and stacking faults are created and consequently, the hardness increases appreciably from 24.2 GPa to 35.6 GPa, while the fracture toughness does not deteriorate.

2. Experimental details

The experiments were performed in a home-made instrument shown in Fig. 1. In order to produce high-density ions, a direct current FCVA (DC-FCVA) was installed on the vacuum chamber. The DC-FCVA consisted of two components: a cathode vacuum arc plasma source and 90°

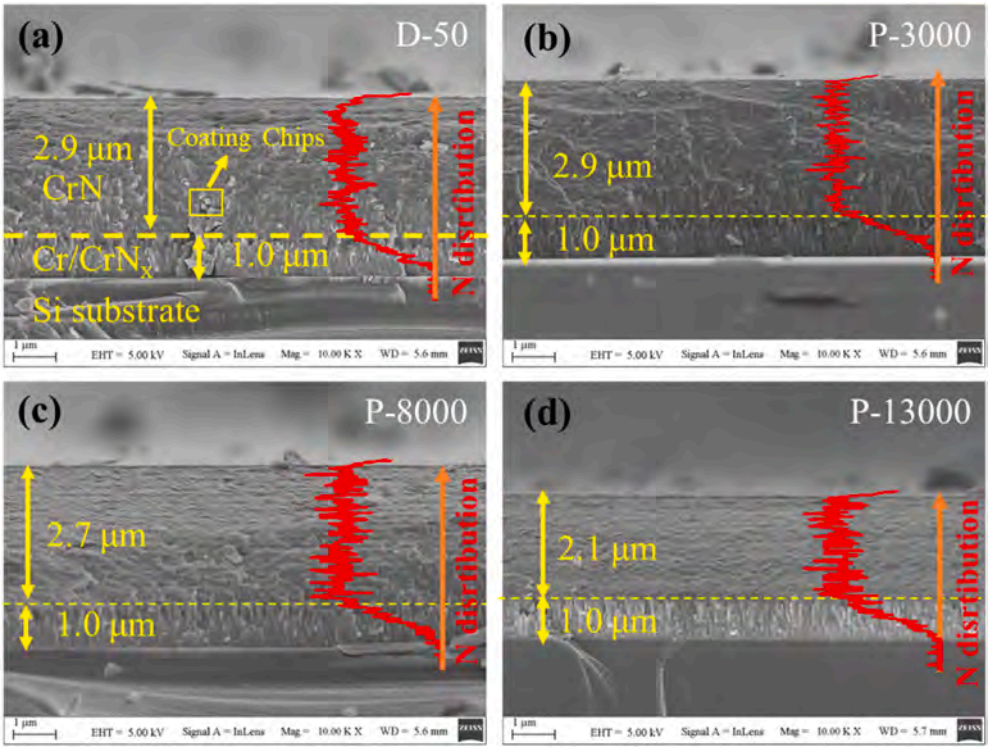

Fig. 2. Cross-sectional morphology of different samples.

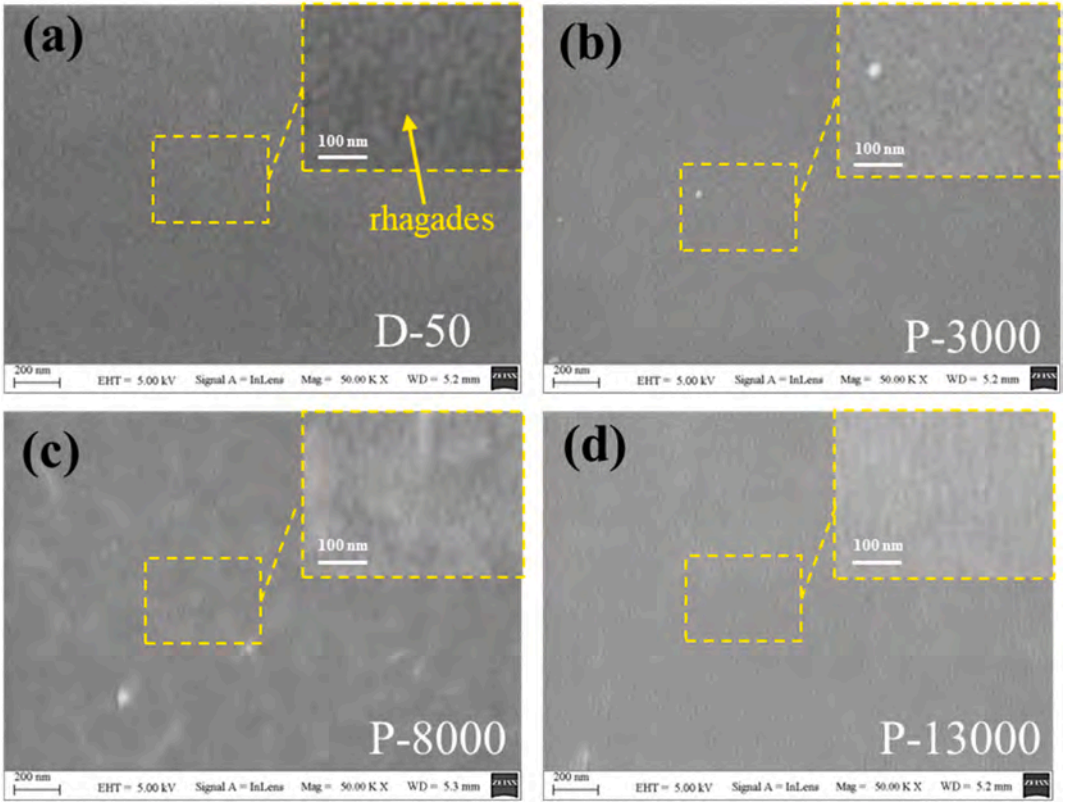

Fig. 3. Surface morphology of different samples.

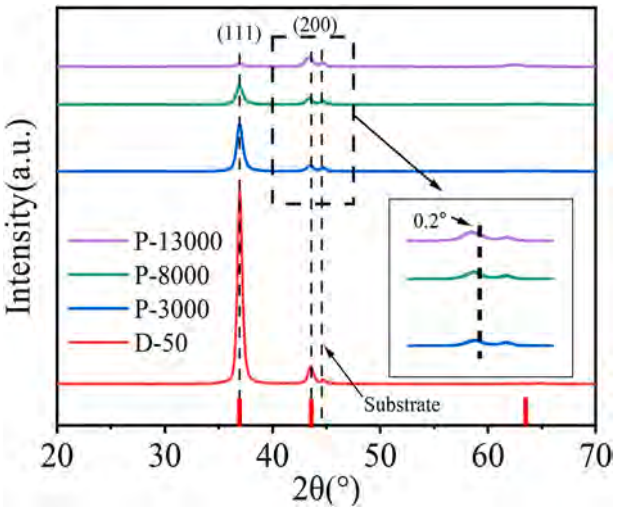

Fig. 4. XRD patterns of the coatings.

curved duct wrapped with electromagnetic coils to generate a magnetic field to guide and transport the plasma out of the duct. The 90° duct blocked metal droplets/atoms and only ions and electrons can enter the vacuum chamber to conduct ion implantation and deposition. The 90° duct was also slightly biased to a low voltage to avoid inadvertent deposition on the interior. The filtered ions were extracted and accelerated to the sample by a substrate bias during ion implantation and deposition. The bias was −50 V DC superimposed with a pulsed high voltage (25 Hz, 20 μs). During DC biasing, the CrN coating was deposited and ion implantation was conducted when the pulsed bias was applied. The DC bias was always on while the pulsed bias was changed to prepare different samples as shown in Table 1. The D-50 sample was deposited at

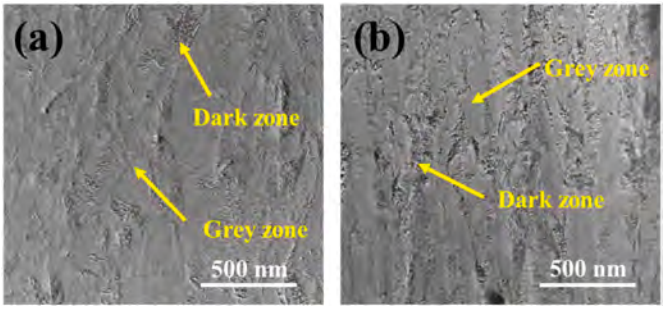

Fig. 5. Cross-sectional morphology observed by TEM: (a) Cross-sectional morphology of D-50; (b) Cross-sectional morphology of P-13000.

a DC bias of −50 V during the whole procedure. The P-3000, P-8000, and P-13000 samples are deposited at −50V DC and respectively implanted at pulsed −3000V, −8000V and −13000V at the same time.

Double-side-polished p-type Si (110) wafers and high-speed steel (HSS) samples were the substrates. Prior to PIII&D, the substrates were cleaned ultrasonically in acetone and alcohol for 30 min. The CrN coatings were deposited using a 99.99% pure conical Cr target with upper and base diameters of 50 and 70 mm, respectively in the Ar (99.999%) and N_2 (99.999%) environment. The cathode current of the DC-FCVA was 50 A. The Ar and N_2 flow rates were 50 sccm and 20 sccm and the residual pressure was 0.7 Pa. Before CrN deposition, a Cr/CrN_x interlayer was deposited to release the residual stress and improve adhesion. The Cr/CrNx interlayer was fabricated by gradually increasing the N_2 flow from 0 sccm to 20 sccm in 25 min at a DC bias of −50 V without the pulsed bias. After Cr/CrN_x was produced, CrN was deposited and/or ion implanted. The whole process took 3 h.

The morphology of the coatings was examined by field-emission scanning electron microscopy (FE-SEM, ZEISIS SUPRA@55). X-ray

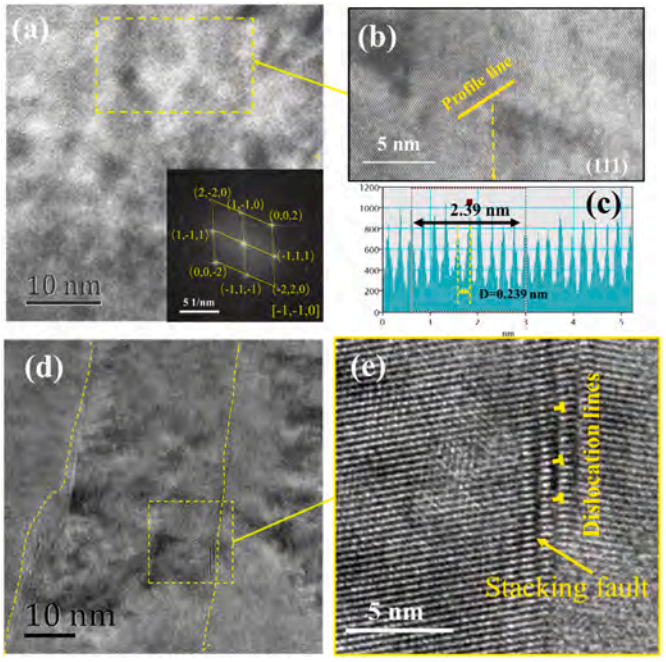

Fig. 6. TEM images of D-50: (a) Typical Zone of the grey area, (b) Enlarged picture of the yellow box in (a), and (c) Profile of the line in (b), (d) Typical Zone of the dark area, (e) Enlarged picture of the yellow box in (d). (For interpretation of the references to colour in this figure legend, the reader is referred to the Web version of this article.)

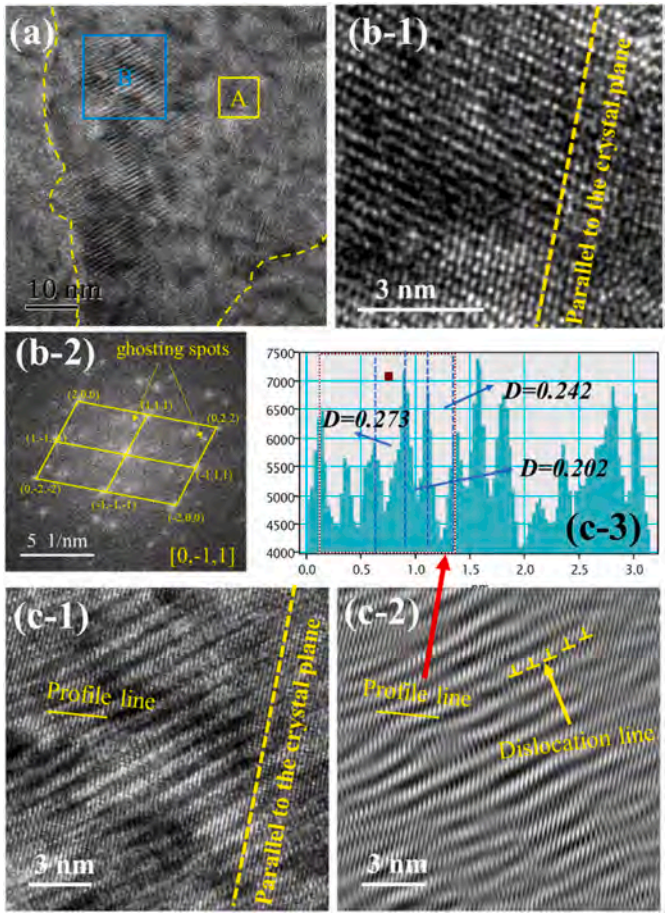

Fig. 7. TEM images of the P-13000: (a) Typical Zone; (b-1) Enlarged picture of zone A in (a); (b-2) SAED pattern of zone A; (c-1) Enlarged picture of zone B in (a); (c-2) FFT of (c-1); (c-2) Profile of the line in (1–2).

diffraction (Bruker, D8 discover) was used to detect the phase structure and crystallinity of the coatings using a step of 0.02° and Cu K_α X-ray (1.5406 Å) at a power of 3200 W. The structural evolution was monitored by transmission electron microscopy (TEM, JEM-3200FS) and the cross-sectioning was performed with a focused ion beam (FIB, FEI Scios). The dislocation density was calculated from the TEM picture. The residual stress was determined on a film stress tester (FST-1000, SuPro Instruments, China) and calculated by Stoney's equation according to the substrate curvature method (SCM) [18,19]. A nano-hardness tester (Hysitron, Ubi-1) was employed to measure the hardness and elastic modulus using a maximum indentation depth of 100 nm. The total indentation depth was no more than 10% of the coating thickness to avoid influence of the substrate [20]. The fracture toughness was evaluated by indentation at a load of 0.98 N on the Vickers hardness tester (HV-1000, Shanghai Jvjing, China). When the Vickers indentation tip indented the coating, cracks perpendicular to the surface emanated from the corners because of the contact impression [21]. A higher toughness sustained higher deformation leading to a shorter crack length and the fracture toughness was calculated by Lawn's equation (Equation (1)) [21]:

$$K_{IC} = \alpha (E/H)^{\frac{1}{2}} \frac{P}{c^{3/2}} \quad (1)$$

where P is the peak load, c is the crack length, α is the empirical constant depending on the type of indenter with that of the Vickers indenter being 0.016, and E and H are the elastic modulus and hardness of the coating, respectively.

3. Results and discussion

The cross-sectional images of the samples are exhibited in Fig. 2. All the samples show the typical double layer structure with a 1 μm thick Cr/CrNx layer and top layers with thicknesses of about 2.9 μm, 2.9 μm, 2.7 μm and 2.1 μm for D-50, P-3000, P-8000, and P-13000, respectively. The declining coating thickness may be attributed to enhanced etching

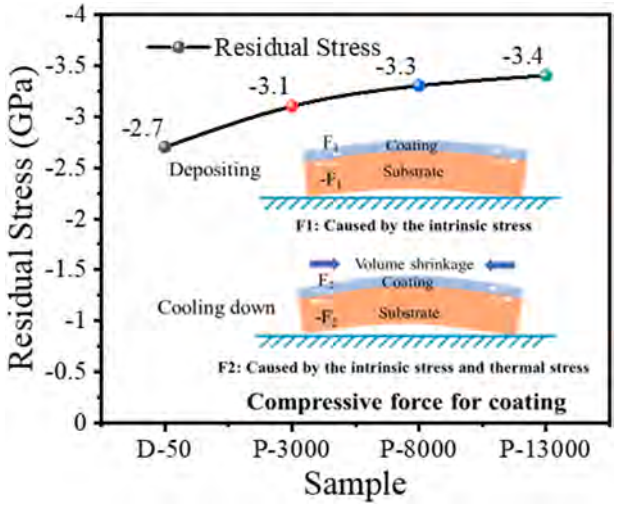

Fig. 8. Residual stress of the samples.

effects at higher biases [22]. The top CrN layers of D-50 sample shows some coatings chips and grain boundaries could be observed around those chips, indicting slightly loose structure. With the increasing implanted bias, the coatings chips disappear and the cross-sections become finer and smoother with increasing pulsed bias indicating higher compactness. The higher compactness could be ascribed to the

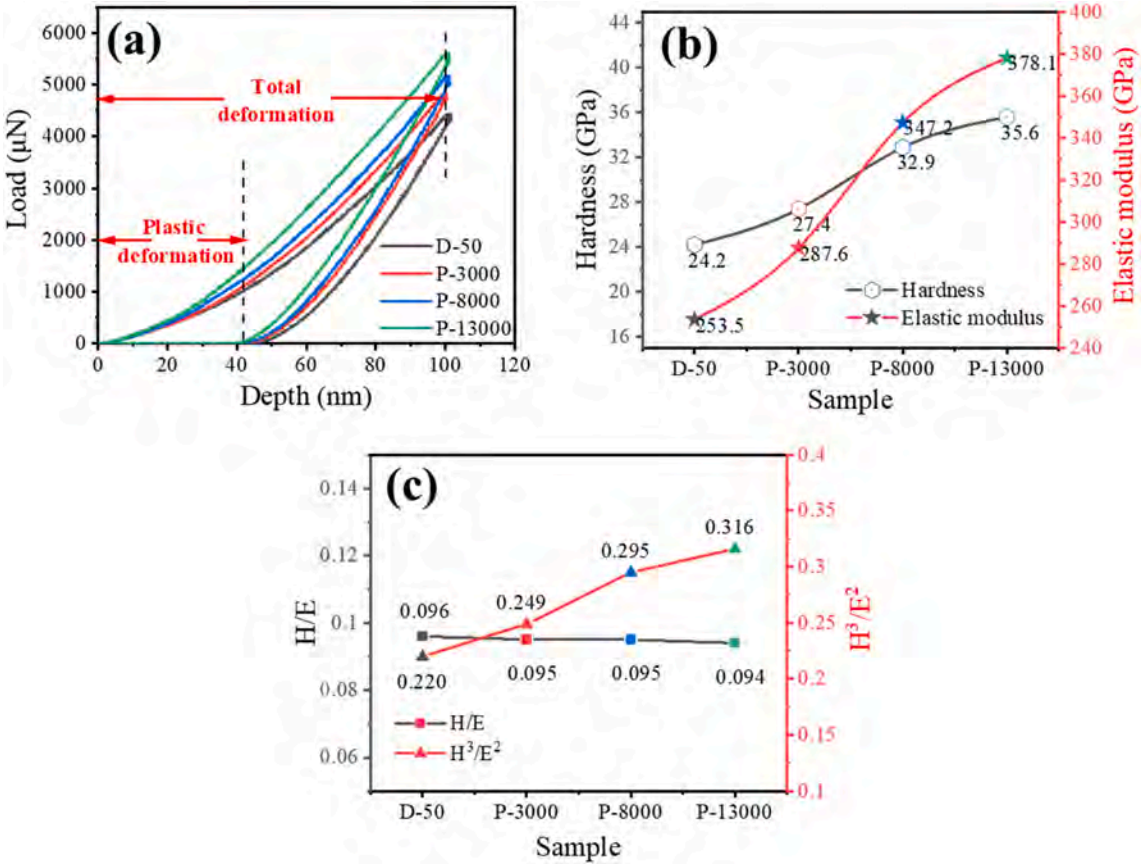

Fig. 9. Mechanical properties of the samples: (a) Load versus depth curves during indentation; (b) H and E; (c) H/E and H^3/E^2.

enhanced ion bombardment accompanied with the ion implantation.

The surface morphology of the samples is displayed in Fig. 3. All the samples show a flat surface without macro-particles due to filtering by the 90° magnetic duct. The droplet-free plasma avoids the shielding effect of metal particles to ensure the ion implantation effects. The surface of D-50 shows tiny grooves in enlarged picture because of stacking of nanograins which is consistent with the loose structure as illustrated in Fig. 2. After ion implantation, the grooves disappear gradually as shown in Fig. 3(c–d) indicating the ion implantation increase the compactness due to ion fill-in and etching by energic ions.

Fig. 4 shows the XRD patterns of the coatings. The diffraction peaks at 37.5° and 43.7° correspond to the (111) and (200) orientations, respectively. The crystal structure can be indexed to face-centred cubic (FCC) structure of the $F_{m\text{-}3m}$ space group (PDF#11–0065). Sample D-50 exhibits a narrow and strong peak at 37.5° indicating preferred growth in the (111) direction. However, the intensity of the (111) peak decreases with increasing pulsed bias. The crystal defects could absorb the X ray and would weak the peak intensity [23,24]. Therefore, the weaken peak intensity may be ascribed to the increased defect intensity with ion implantation. The (200) peak from D-50 sample is at the theoretical position, whereas the peaks of other samples shift gradually to a small angle with a positive correlation with the pulsed bias. According to Bragg's equation, the smaller angle indicates larger interplanar crystal spacing due to insertion of implanted ions.

The cross-sectional morphology of D-50 and P-13000 after FIB is examined by TEM as shown in Fig. 5(a) and 5(b). Fig. 5(a) shows high contrast in different areas with about 70% grey zone and 30% dark zone. However, the percentage of the darker zone increases to about 75% for P-13000 as shown in Fig. 5(b). The dark zones in the TEM micrographs arise from lower electron transmission [25]. Since the materials and thickness are similar, reduced electron transmission may be caused by absorption and scattering by crystal defects, which is consistent with the weaker diffraction peaks of P-13000.

The change in the crystal lattice is monitored by TEM. The typical morphology of D-50 in the grey area (in Fig. 5(a)) is presented in Fig. 6 (a). The selected-area electron diffraction (SAED) pattern reveals the crystal belt axis is [−1, −1, 0], which is corresponding to a plane spacing of 0.239 nm. The magnified picture of zone A in Fig. 6(a) is displayed in Fig. 6(b). The lattice fringe is clear and distributed uniformly and orderly without obvious defects. The interplanar crystal spacing is derived by measuring 10 adjacent 10 lattice fringes on the yellow line in Fig. 6(b) and the height fluctuation is displayed in Fig. 6(c). The average spacing is about 0.239 nm which is equal to the theoretical interplanar spacing. The morphology of the dark areas (in Fig. 5(a)) was also observed and depicted in Fig. 6(d). Fig. 6(d) presents an irregular lattice fringe, indicting the appearance of crystal defects. The enlarged picture in Fig. 6(e) reveals there are some tiny stacking faults mixed with dislocations around the grain boundaries. The appearance of the defects explained the colour contrast change of different areas in Fig. 5(a). The calculated density of dislocation was about $5.2 \times 10^{14}/m^2$, which is low because the small proportion of the dark area in Fig. 5(a).

TEM image of P-13000 is different from that of D-50 sample as shown in Fig. 7. Two morphologies are discerned in Fig. 7(a): a smooth one and the other being wavy marked by yellow and blue boxes. The enlarged pictures of these two zones are displayed in Fig. 7(b–c). Figs. 7(b-1) shows the morphology of the yellow box in Fig. 7(a). Although the basic lattice fringes can be observed, most of the atoms are displaced from the original position forming a cluster of point defects. Those point defects may be caused by the ion inserting and replacement of the crystal lattice during the ion implantation. The selected-area electron diffraction (SAED) pattern of zone A shows ghost spots in Fig. 7(b-2) indicating the existence of distorted atoms near the equilibrium position [26]. Those defects and the resulting crystal lattice change impose resistance to dislocation propagation and meanwhile improves the chances for

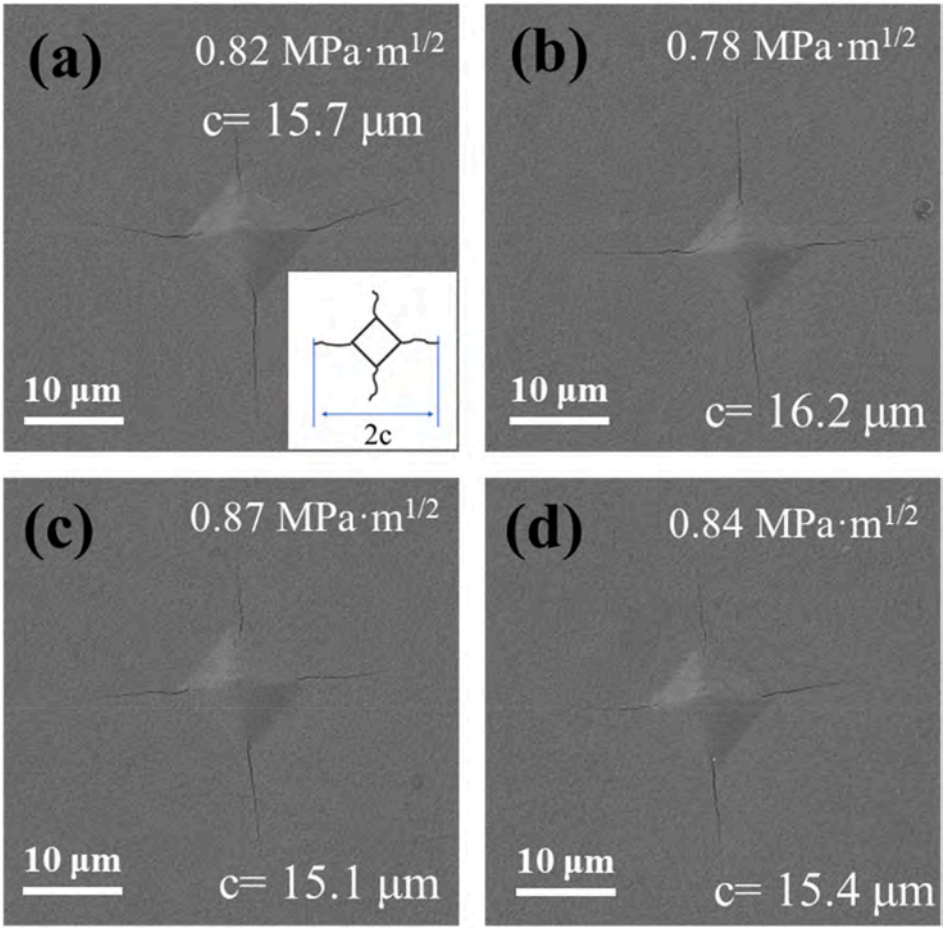

Fig. 10. Indentation cracks after the fracture toughness test.

dislocation interlocking and accumulation, which is particularly useful for the mechanical enhancement [27,28]. The enlarged image of zone B shows obvious wavy Moire fringes as shown in Fig. 7(c) suggesting that stacking faults are generated by ion implantation. In order to clearly display the Moire fringes, fast Fourier transform (FFT) is performed on Figs. 7(c-1) and the results are presented in Figs. 7(c-2). The fringes are distorted severely and some dislocations are distributed near the convex fringes. The density of the dislocation lines reaches $1.3 \times 10^{17}/m^2$ which was much higher than the D-50 samples, consistent with the increased dark areas. The profile along the yellow line is displayed in Figs. 7(c-3). Owing to large distortion, the planar spacing shows a range between 0.202 and 0.273 nm. The average planar spacing is about 0.242 nm which is larger than the theoretical value (0.239 nm), which is consistent with the peak shift in XRD. Previous studies have proofed the stacking faults could widely separate the dislocations pile-up and pin the dislocations [29,30]. Therefore, the mechanical properties were promising to enhance.

Fig. 8 shows the residual stress of each sample. The residual stress is mainly caused by intrinsic and thermal stress. Intrinsic stress is produced by crystal defects, phase transition, and so on during film growth [31–33], whereas thermal stress is caused by the different thermal expansion coefficients (CTE) of the substrate and coatings [34]. Because the deposition temperature is the same for all the samples, the difference in the residual stress is mainly caused by the intrinsic stress in lieu of the thermal stress. D-50 show a compressive stress of −2.7 GPa. However, when the pulsed bias is applied, high-density crystal defects are produced as shown in Fig. 7. The implanted atom would expand the interplanar spacing and the coating volume as revealed in Fig. (7). Higher implanted bias would create better implantation effect and larger interplanar spacing. However, the coating size was restrained by the substrate, therefore the coating would sustain a compressive stress. The larger interplanar spacing results in higher compressive stress between grains as well as bending of the substrate as shown in the inset. Our results show that the residual stress increases gradually to −3.1 GPa, −3.3 GPa, and −3.4 GPa for P-3000, P-8000 and P-13000, respectively.

The mechanical properties of the coatings are determined and shown in Fig. 9. The load *vs.* depth curve is displayed in Fig. 9(a). The maximum load increases from 4300 nN to 6300 nN with pulsed biasing reflecting enhanced resistance to deformation. In addition, plastic deformation during indentation is similar for all the samples with a ranging of 41–45 nm and therefore, the plasticity is not sensitive to the pulsed bias. The hardness(H) and elastic modulus (E) calculated from the load versus depth curve are presented in Fig. 9(b). The hardness (H) increases significantly from 24.2 GPa to 35.6 GPa with increasing pulsed bias. Meanwhile, the elastic modulus (E) exhibits a similar rise with H, reaching 378.1 GPa for P-13000. The increased hardness could be attributed to the increased crystal defects, which imposes resistance to dislocation propagation and meanwhile improves the chances for dislocation interlocking and accumulation, which is particularly useful for the mechanical enhancement [28,29]. The H/E ratio can be used to quantify the elastic strain to failure and the H^3/E^2 ratio represents the resistance to plastic deformation, which determines the toughness of the materials [35]. Normally, the hardness increase is accompanied by deteriorating toughness. Here, as the pulsed voltage goes up, the H/E ratio stabilizes at 0.095 and the H^3/E^2 ratio rises slightly from 0.220 GPa to 0.316 GPa, indicating that the toughness of the CrN coatings does deteriorate with increasing hardness.

Fig. 10 presents the morphology of the indentation in fracture

toughness test. Obvious cracks can be observed from the corner revealing crack progression under the load. The average crack lengths (c) at the four corners are 15.7 μm, 16.2 μm, 15.1 μm, and 15.4 μm for D-50, P-3000, P-8000 and P-13000, respectively. According to the crack lengths, the fracture toughness of each sample is also similar being 0.82 MPa $m^{1/2}$, 0.78 MPa $m^{1/2}$, 0.87 MPa $m^{1/2}$ and 0.84 MPa $m^{1/2}$. The fracture toughness is stable and does not decrease with increasing hardness. Generally, initiation and propagation of cracks are related to pile-up of dislocations at the grain boundaries. When extended screw dislocation intersects a planar defect or boundary under an applied stress, the dislocation can directly traverse across them with the incoming screw being absorbed into the planar defect or boundary and then desorbed through cross-slip [4,29]. Stacking faults could release the dislocation pile-up [27,29]. As a result, the chance of crack initiation does not increase and the fracture toughness does not worsen.

4. Conclusion

Plasma immersion ion implantation and deposition (PIII&D) is performed to introduce crystal defects in CrN coatings. Different pulsed biases are supplied on top of −50 V DC to perform energetic ion implantation and deposition in concert. TEM reveals that high-density defects are created in the ion-implanted samples. Compared to sample D-50, the dislocation density of P-13000 sample significantly increased from $5.2 \times 10^{14}/m^2$ to $1.3 \times 10^{17}/m^2$. In addition, the covered area of defects increased from 30% to 75% with the ion implantation. As a result, the hardness of the coating increases significantly from 24.2 GPa to 35.6 GPa and more importantly, the fracture toughness is not compromised. The strategy and results provide guidance on how to strengthen coatings by energetic ion beam bombardment and defect engineering.

CRediT authorship contribution statement

L.L. Liu and **T.J. Li**: Conceptualization, Methodology, Writing – original draft; **Z.Z. Wu**: Resources, Writing – review & editing; **Q.D. Ruan**, **Y.H. Ma, C. Huang**, **Y.Z. Wu, X. L. Zhang** and **D. Li**: Data analysis, Discussions: **Z.C. Wu** and **R.K.Y. Fu:** Resources; **P.K. Chu**: Supervision, Resources, Writing – review & editing.

Declaration of competing interest

The authors declare that they have no known competing financial interests or personal relationships that could have appeared to influence the work reported in this paper.

Acknowledgements

This work was financially supported by the Shenzhen Science and Technology Research Grants [JSGG20191129112631389], City University of Hong Kong Strategic Research Grant (SRG) [7005505], Shenzhen – Hong Kong Innovative Collaborative Research and Development Program [SGLH20181109110802117 and CityU 9240014], and City University of Hong Kong Donation Research Grant [grant number DON-RMG 9229021].

References

[1] B. Fotovvati, N. Namdari, A. Dehghanghadikolaei, On coating techniques for surface protection: a review, J. Manuf. Mater. Proc. 3 (2019) article 28.
[2] F.S. Mei, Z.J. Zhang, Y. Yu, et al., Microstructure, mechanical, tribological, and oxidizing properties of AlCrSiN/AlCrVN/AlCrNbN multilayer coatings with different modulated thicknesses, Ceram. Int. 49 (2022) in press.
[3] X. Li, K. Lu, Improving sustainability with simpler alloys, Science 364 (2019) 733–734.
[4] K. Lu, L. Lu, S. Suresh, Strengthening materials by engineering coherent internal boundaries at the nanoscale, Science 324 (2009) 349–352.
[5] K. Lu, Stabilizing nanostructures in metals using grain and twin boundary architectures, Nat. Rev. Mater. 1 (2016) (2016), article 16019.
[6] M. Mori, K. Yamanaka, S. Sato, et al., Strengthening of biomedical Ni-free Co-Cr-Mo alloy by multipass "low-strain-per-pass, Acta Biomater. 28 (2015) 215–224.
[7] S.Q. Zhu, H.G. Yan, X.Z. Liao, et al., Mechanisms for enhanced plasticity in magnesium alloys, Acta Mater. 82 (2015) 344–355.
[8] H. Windischmann, Intrinsic stress in sputtered deposited thin films, Crit. Rev. Solid State Mater. Sci. 9 (1992) 547–596.
[9] J. Salamania, L.J.S. Johnson, I.C. Schramm, et al., Influence of pulsed-substrate bias duty cycle on the microstructure and defects of cathodic arc-deposited Ti1-xAlxN coatings, Surf. Coat. Technol. 419 (2021), 127295.
[10] Z. Xu, Z.L. Zhang, M. Bartosik, et al., Insight into the structural evolution during TiN film growth via atomic resolution TEM, J. Alloys Compd. 754 (2018) 257–267.
[11] L.L. Liu, Q.D. Ruan, Z.Z. Wu, et al., Hard and tough CrN coatings strengthened by high-density distorted coherent grain boundaries, J. Alloys Compd. 894 (2021) article 162139.
[12] E. Chason, S.T. Picraux, J.M. Poate, et al., Ion beams in silicon processing and characterization, J. Appl. Phys. 81 (1997) 6513–6561.
[13] B. Deng, T. Ye, H.L. Liu, et al., Influence of niobium ion implantation on the microstructure and tribological properties of TiAlN coatings, Surf. Coat. Technol. 228 (2013) S554–S557.
[14] A. Olofinjana, T. Tesfamichael, J.M. Bell, Chemical modification and the attending surface hardness of low alloy steel through medium energy nitrogen ion implantation, J. Mater. Process. Technol. 164–165 (2005) 905–910.
[15] B. Tian, W. Yue, C.B. Wang, et al., Surface properties of W-implanted TiN coatings post-treated by low temperature ion sulfurization, Appl. Surf. Sci. 353 (2015) 1156–1163.
[16] H. Trombini, M. Vos, R.G. Elliman, et al., Depth profiling of ion-implanted samples by high-energy electron scattering, J. Phys. D Appl. Phys. 53 (2020), 135304 article.
[17] A.G. Liu, X.F. Wang, B.Y. Tang, et al., A novel distributed system for plasma immersion ion implanter control and automation, Rev. Sci. Instrum. 69 (1998) 1495–1498.
[18] G.G. Stoney, The tension of metallic films deposited by electrolysis, in: Proceedings of the Royal Society of London. Series A 82, 1909, pp. 172–175.
[19] L.L. Liu, Q.D. Ruan, Z.Z. Wu, et al., Fabrication and cutting performance of CrAlN/CrAl multilayer coatings deposited by continuous high-power magnetron sputtering, Ceram. Int. 48 (2022) 14528–14536.
[20] L.L. Liu, W. Tang, L. Zhou, et al., Comparative study of TiAlN coatings deposited by different high-ionization physical vapor deposition techniques, Surf. Coat. Technol. 46 (2020) 10814–10819. Ceram. Int.
[21] B. Lawn, D. Marshall, Hardness, toughness, and brittleness: an indentation analysis, J. Am. Ceram. Soc. 62 (1979) 347–350.
[22] S. Gangopadhyay, R. Acharya, A.K. Chattopadhyay, et al., Effect of substrate bias voltage on structural and mechanical properties of pulsed DC magnetron sputtered TiN-MoSx composite coatings, Vacuum 84 (2010) 843–850.
[23] I. Booker, L.R. Khoshroo, J.F. Woitok, et al., Dislocation density assessment via X-ray GaN rocking curve scans, Phys. Status Solidi C 7–8 (2010) 1787–1789.
[24] Z. Cong, Y. Murata, Dislocation density of lath martensite in 10Cr-5W heat-resistant steels, Mater. Trans. 52 (2011) 2151–2154.
[25] J. Holm, B. Caplins, J. Killgore, Obtaining diffraction patterns from annular dark-field STEM-in-SEM images: towards a better understanding of image contrast, Ultramicroscopy 212 (2020), 112972.
[26] N. Nitta, T. Hasegawa, H. Yasuda, et al., Void formation and structure change induced by heavy ion irradiation in GaSb and InSb, Mater. Trans. 51 (2010) 1059–1063.
[27] P. Müllner, C. Solenthaler, P. Uggowitzer, et al., On the effect of nitrogen on the dislocation structure of austenitic stainless steel, Mater. Sci. Eng., A 164 (1–2) (1993) 164–169.
[28] J.S. Robach, I.M. Robertson, B.D. Wirth, et al., In-situ transmission electron microscopy observations and molecular dynamics simulations of dislocation–defect interactions in ion irradiated copper, Philos. Mag. A 83 (955) (2003) 955–967.
[29] Y. Yue, Y. Gao, W. Hu, et al., Hierarchically structured diamond composite with exceptional toughness, Nature 582 (2020) 370–374.
[30] H. Li, H. Zong, S. Li, et al., Uniting tensile ductility with ultrahigh strength via composition undulation, Nature 604 (2022) 273–279.
[31] S.C. Seel, C.V. Thompson, Tensile stress generation during island coalescence for variable island-substrate contact angle, J. Appl. Phys. 93 (2003) 9038–9042.
[32] N.A. Marks, J.M. Bell, G.K. Pearce, et al., Atomistic simulation of energy and temperature effects in the deposition and implantation of amorphous carbon thin films, Diam. Relat. Mater. 12 (2003) 2003–2010.
[33] R.W. Hoffman, Stresses in thin films: the relevance of grain boundaries and impurities, Thin Solid Films 34 (1976) 185–190.
[34] J. Lin, R. Wei, A comparative study of thick TiSiCN nanocomposite coatings deposited by dcMS and HiPIMS with and without PEMS assistance, Surf. Coat. Technol. 338 (2018) 84–95.
[35] A. Leyland, A. Matthews, On the significance of the H/E ratio in wear control: a nanocomposite coating approach to optimised tribological behaviour, Wear 246 (2000) 1–11.